# Computation of trailing-edge aeroacoustics with vortex shedding

**By M. Wang**

## 1. Motivation and objectives

The prediction and control of noise generated by turbulent flow past the trailing edge of a lifting surface continue to be of considerable interest. In aeronautical applications, there has been increasing attention to trailing-edge noise as evidenced by the proliferation of papers devoted to this topic in the annual AIAA Aeroacoustics Conferences in recent years. This is due to the significant advances made in jet noise reduction, which causes other noise sources, such as turbo-fan engines and the airframe, to rise in importance. Trailing-edge noise is often a significant contributor to these noise components. In naval applications, the noise generated by the trailing edges of marine propellers and hydrofoils is a serious concern. Trailing-edge noise also arises from wind turbines, axial and centrifugal fans in rotating machines, and helicopter rotors.

It is well known that an unsteady flow in free space is a relatively inefficient noise source of quadrupole nature in the low-Mach-number limit (Lighthill 1952). The presence of a solid object in the flow, such as an airfoil, enhances noise radiation in two ways: (i) by creating or augmenting noisy flow features such as unsteady separation and vortex shedding and (ii) by imposing a boundary inhomogeneity that promotes efficient conversion of flow energy to acoustic energy. The theoretical framework for trailing-edge noise, valid for airfoils that are long and thin relative to the acoustic wavelength, has long been established based on the half-plane diffraction theory (see, for example, Ffowcs Williams & Hall 1970; Howe 1978). A number of computational studies were performed in recent years using Lighthill's theory (Lighthill 1952) in conjunction with large-eddy simulation (LES) of the near field (Wang & Moin 2000; Manoha, Troff & Sagaut 2000; Oberai, Roknaldin & Hughes 2002). Wang & Moin (2000) computed the flow over a model airfoil studied experimentally by Blake (1975) at chord Reynolds number of $2.1 \times 10^6$, and obtained reasonable agreement with experimental measurements in terms of velocity and unsteady surface pressure statistics. The trailing edge, with a tip angle of 25°, was relatively sharp and hence did not produce coherent vortex shedding. Since no acoustic-field measurement was taken in Blake's experiment, it was not possible to make a quantitative assessment of the computed far-field data. In addition, the fidelity of the velocity boundary conditions employed in the LES is questionable because of wind tunnel installation effects present in the experiment, which can cause the flow to deviate from that in free space (Moreau *et al.* 2003).

To provide a comprehensive data set for validating computational results and studying noise source mechanisms, a new experiment was started at the University of Notre Dame. Data from preliminary measurements recently became available (Olson & Mueller 2004; Shannon & Morris, personal communication), which provide an opportunity to revisit the trailing-edge noise problem with close coordination with the ongoing experimental work. The new trailing edge is more blunt than the one considered previously (Wang & Moin 2000). With a tip-angle of 45°, it produces coherent vortex shedding in addition

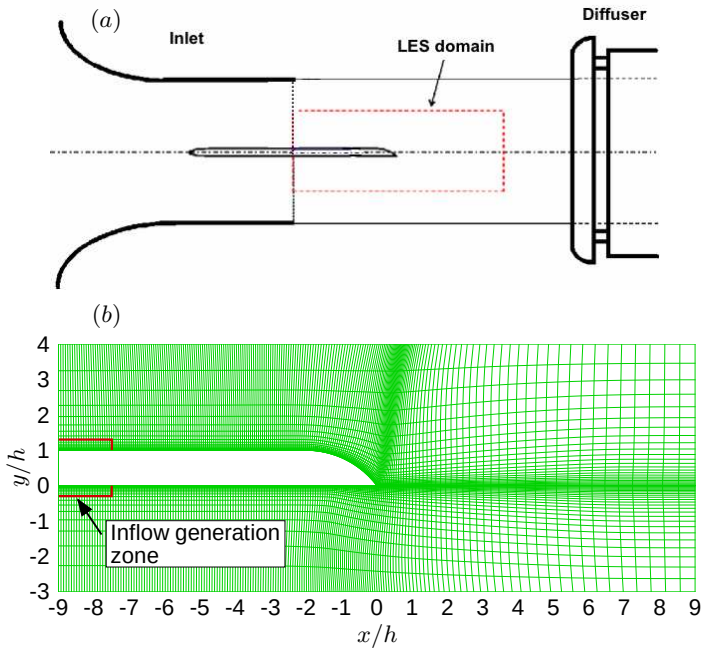


FIGURE 1. Experimental and computational configurations. ($a$) Setup in the Notre Dame open-jet facility (Olson & Mueller 2004). ($b$) Computational grid with 1/4 grid lines plotted.

to the scattering of the turbulent boundary-layer eddies, both significant noise sources. The primary objective of this study is to evaluate the LES predictions of a trailing-edge flow with vortex-shedding and the associated noise against experimental measurements. The computational results and validation are summarized in this report. For the first time to our knowledge, we present a direct comparison of the radiated trailing-edge noise spectra obtained from computational and experimental studies under closely matched flow conditions.

## 2. Accomplishments

### 2.1. *Configuration and computational approach*

The experimental flow configuration is shown in Fig. 1$a$. A 45°, asymmetrically beveled trailing edge is attached to a flat strut with an elliptical leading edge. The model airfoil, with a chord to thickness ratio of $C/h = 18$, is half-way inside the nozzle in an open-jet anechoic wind tunnel facility. The Reynolds number based on chord and incoming free-stream velocity $U_0$ is $1.9 \times 10^6$, and the free stream Mach number $M \approx 0.09$. The span of the airfoil is $12h$, and the flow is considered statistically two-dimensional.

Large-eddy simulations are performed in a computational domain bounded by the dashed lines in Fig. 1$a$. As in Wang & Moin (2000), only the aft section (one half of the chordlength in this case) of the airfoil is included to save computational cost and bypass the difficulty with leading-edge transition (Wang *et al.* 2004). The computational domain size is $18h$ (streamwise, $x$) $\times$ $7h$ (normal, $y$) $\times$ $h$ (spanwise, $z$). The computational grid, defined in curvilinear coordinates in the $x$-$y$ plane (see Fig. 1$b$, where only one in every four grid lines is plotted) and uniform Cartesian coordinate in $z$, uses a total of

$1536 \times 96 \times 96$ points. Of the 1536 streamwise grid points, 640 are distributed along the upper surface, 512 along the lower surface, and $2 \times 192$ along the wake line (branch cut). The near-wall grid resolution is generally (except in a small region around the skin friction peak) $\Delta x^+ \leq 70$, $\Delta y^+ \leq 2$, and $\Delta z^+ \leq 50$ in wall units. This resolution is comparable to that employed by Wang & Moin (2000), which was shown to predict well the trailing-edge flow in Blake's (1975) experiment.

The locations of the top and bottom boundaries are chosen where velocity fluctuations arising from the airfoil wake and the jet shear layers are relatively small, so that steady (mean) velocity boundary conditions (BCs) can be applied. We employed two sets of mean velocity BCs for the inlet, top, and bottom boundaries. One is from the experimental measurement of Olson & Mueller (2004), and the other from a Reynolds-averaged Navier-Stokes (RANS) calculation in a large domain containing the entire airfoil, the nozzle, and the jet. On the rest of the boundaries, the no-slip condition is imposed on the airfoil surface, convective outflow condition in the exit plane, and periodic BC in the spanwise direction.

The numerical method is essentially the same as described in Wang & Moin (2000). It employs an energy-conservative, hybrid finite-difference/spectral Navier-Stokes solver in conjunction with the dynamic subgrid-scale model. The code has been enhanced with a turbulent inflow generation capability employing the "rescale and recycle" technique of Lund, Wu & Squires (1998). The sizes of the recycle regions, marked approximately in Fig. 1*b*, are $(8.5 \times 1.5)\delta$ in the $x$-$y$ plane, where $\delta$ is the inlet boundary-layer thickness. With this approach, time-dependent inflow data in the turbulent boundary layers are generated concurrently with the main simulation, and there is no need for separate simulations and large data files as in our previous work. This procedure proved to be particularly convenient for a related study (Marsden *et al.* 2005) where LES was coupled with an optimization technique to design trailing-edge shapes that minimize noise radiation. In the optimization process many iterations were required on the trailing-edge shape, each with its distinct inlet boundary-layer properties, and thus being able to generate inflow data "on the fly" was important. The momentum-thickness Reynolds numbers of the upper and lower surface boundary layers at the inlet are fixed at 1895 and 1760, respectively, based on experimental values.

### 2.2. *Flow field validation*

The first simulation was conducted using the mean streamwise and normal velocity data ($U$ and $V$) provided by cross-wire measurements (Olson & Mueller 2004) as BCs at the inlet, top and bottom boundaries (the spanwise velocity $W$ was set to zero). However, a large discrepancy was observed between the computed airfoil loading and the experimental value, as shown in Fig. 2. A RANS calculation using the same mesh and BCs as for the LES revealed a similar discrepancy with the experimental $C_p$. To investigate the cause of these discrepancies, another RANS calculation was conducted in a large computational domain which included the entire airfoil and the jet nozzle. The resulting $C_p$ showed a much better agreement with experimental values, suggesting that the velocity field from the large-domain RANS might provide better BCs for the LES in terms of matching the correct airfoil loading. Using these RANS BCs, LES indeed gave a more accurate $C_p$ distribution (cf. Fig. 2).

Figure 3 shows mean streamwise velocity profiles across the upper-surface boundary layer (Fig. 3*a*) and the wake (Fig. 3*b*), at select streamwise stations indicated on the curves. The trailing edge is located at $(x, y) = (0, 0)$. LES results based on experimental and RANS BCs are compared with the profiles measured experimentally. Apparently,

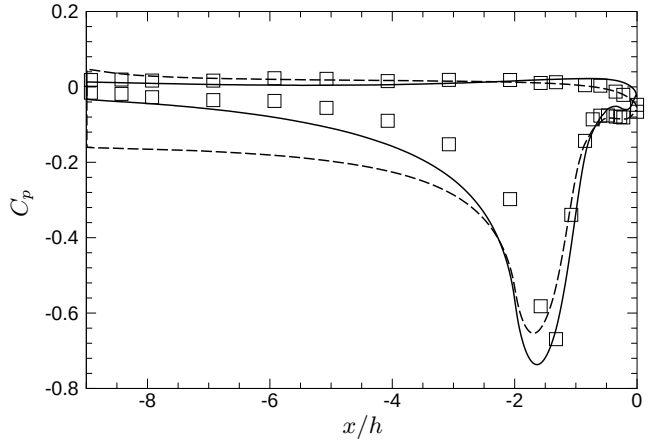


FIGURE 2. Pressure coefficient along the trailing-edge surface. ——— , LES with RANS BCs; - - - - , LES with experimental BCs; □ , Experiment (Olson & Mueller 2004).

the LES profiles using RANS BCs are in better overall agreement with the experimental data, particularly in the trailing-edge region, which is consistent with observations made about the pressure coefficients. The underlying reason can at least partially be explained from the wake profiles in Fig. 3*b*. The velocity profiles from the LES with experimental BCs give smaller mass fluxes ($\int U dy$) across the constant $x$-planes than the mass fluxes of the experimental wake profiles. Based on a global mass balance in the computational domain (cf. Fig. 1), one can deduce that the experimental BCs at the top, bottom and/or inlet boundaries do not provide sufficient mass fluxes into the control volume, since the numerical scheme is strictly mass conservative. Given the large size of the top and bottom boundaries, this mass imbalance could easily be caused by small measurement errors in $V$ on these boundaries. The RANS boundary conditions, on the other hand, give wake mass fluxes consistent with the experimental wake profiles. Other possible reasons for the velocity discrepancies between the LES and experiment are the small velocity fluctuations on the top and bottom boundaries which are present in the experiment but neglected in the computation.

In Fig. 4 the root-mean-square (rms) values of streamwise velocity fluctuations at the same wake stations as in Fig. 3 are plotted. The two LES calculations using experimental and RANS BCs are of comparable accuracy. Both show good agreement with experimental data in terms of maximum turbulence intensity but the LES profiles show a somewhat narrower wake, indicting an underprediction of turbulent mixing.

Since the LES with RANS BCs gives a better overall prediction of the velocity field, it is used in the following discussion and acoustic calculations. One of the concerns in our previous work (Wang & Moin 2000) was the small spanwise domain size $L_z$ which, at $0.5h$, was smaller than the spanwise correlation lengths in the wake and in the separated boundary layer near the trailing edge. This issue has been reexamined in the present simulation. The spanwise domain size employed here is twice that in the previous case, and its effect on the current trailing-edge flow is illustrated in Fig. 5 by comparison with a simulation with the original spanwise domain size in terms of wake turbulence intensities. The smaller domain gives rise to too strong a $u_{rms}$ peak associated with the shear layer emanating from the pressure-side boundary layer, which persists over a large distance in the downstream direction. This suggests that the wake is dominated by two-dimensional

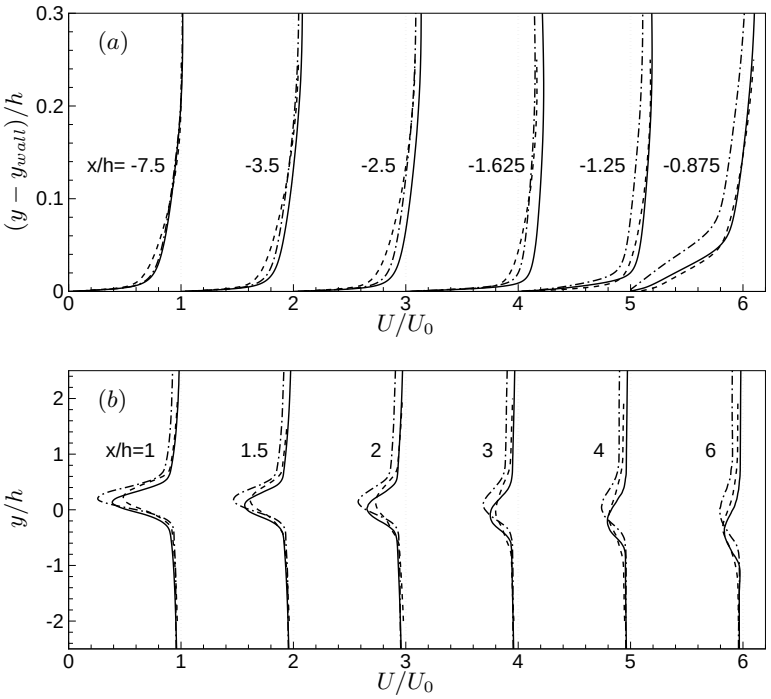


FIGURE 3. Mean streamwise velocity profiles at select streamwise locations in ($a$) the upper-surface boundary layer and ($b$) the wake. ——— , LES with RANS BCs; —·— , LES with experimental BCs; - - - - , Experiment (Olson & Mueller 2004). Individual profiles are shifted horizontally by (from left to right) 0, 1, ..., 5.

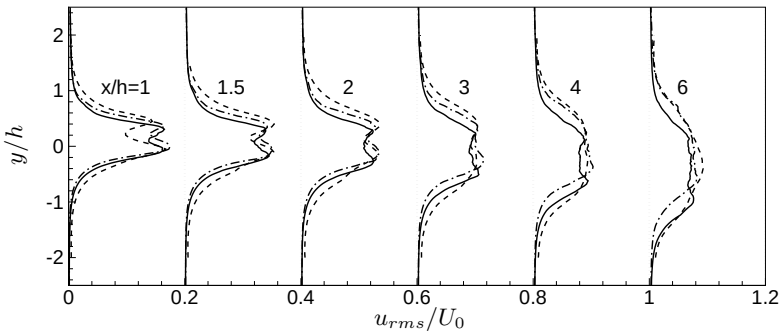


FIGURE 4. Profiles of the rms of streamwise velocity fluctuations at select streamwise locations in the wake. ——— , LES with RANS BCs; —·— , LES with experimental BCs; - - - - , Experiment (Olson & Mueller 2004). Individual profiles are shifted horizontally by (from left to right) 0, 0.2, ..., 1.0.

vortices. On the other hand, the boundary-layer velocity profiles and airfoil loading are found to be little affected by the smaller spanwise domain size and, as will be shown in Section 2.3, the effect on the radiated sound power spectra is relatively small.

Figure 6 depicts the iso-contours of the streamwise velocity in a given spanwise plane at a given time instant. It clearly shows large coherent structures in the wake as a result

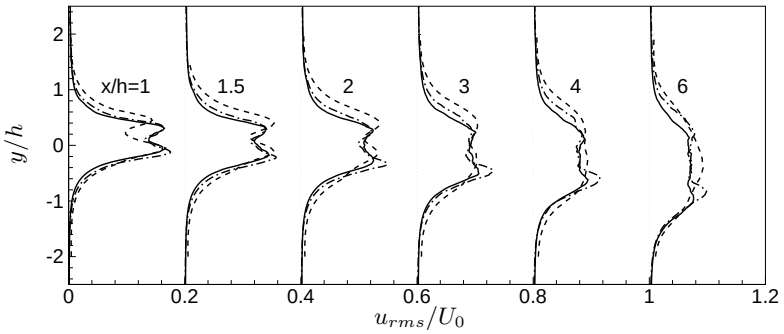


FIGURE 5. The effect of spanwise domain size $L_z$ in LES on the rms of streamwise velocity fluctuations in the wake. ——— , $L_z = h$; —·— , $L_z = h/2$; - - - - , Experiment (Olson & Mueller 2004). Individual profiles are shifted horizontally by (from left to right) 0, 0.2, ..., 1.0.

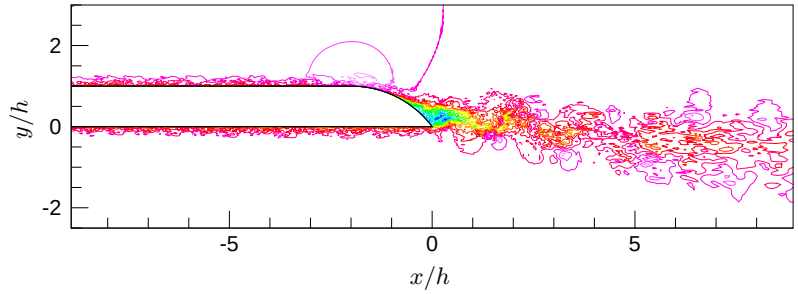


FIGURE 6. Instantaneous streamwise velocity $u/U_0$ in a given spanwise plane. Contour levels are from $-0.3$ to 1.2 with increment of 0.1.

of vortex shedding, as well as realistic small-scale turbulence. The shedding frequency is most easily determined from the energy spectra of the streamwise and normal velocity components shown in Fig. 7. The Strouhal number of vortex shedding is $fh/U_0 \approx 0.44$, compared to the value of 0.40 determined from the experiment. In addition to the major shedding peak, a secondary peak at twice the shedding frequency is also apparent in the spectra.

It is of interest to examine the behavior of the fluctuating velocity components normal to the trailing edge since they provide the predominant acoustic source (Ffowcs Williams & Hall 1970). The spatial distributions of their rms values in the vicinity of the trailing edge are plotted in Fig. 8. The $u_{rms}$ contours exhibit two regions of high intensity that are associated with the two shear layers from the upper and lower surfaces of the airfoil. The fluctuations arising from the lower shear-layer are particularly intense, underscoring the key role played by the attached boundary layer on the pressure side in sound generation. High levels of normal velocity fluctuations $v_{rms}$ are concentrated in a single region near the lower surface of the edge.

### 2.3. *Noise calculation*

The acoustic far field is computed using a simplified form of the Ffowcs Williams & Hall (1970) solution to the Lighthill equation as described by Wang & Moin (2000). This approach is based on an approximate Green's function for a rigid half-plane and

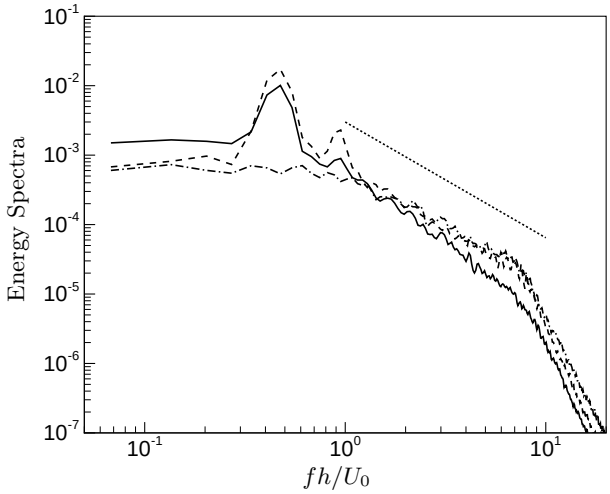


FIGURE 7. Energy spectra as a function of frequency at near-wake location $x/h = 0.5$, $y/h = 0$. ——— , $E_{uu}/U_0h$; – – – – , $E_{vv}/U_0h$; —·— , $E_{ww}/U_0h$; ····· , line with $-5/3$ slope.

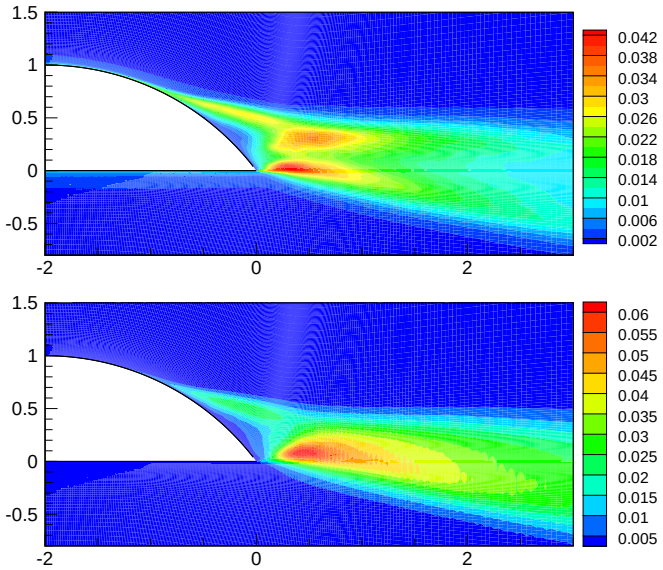


FIGURE 8. Root-mean-square of velocity fluctuations. Top: streamwise component ($u_{rms}/U_0$); Bottom: normal component ($v_{rms}/U_0$).

is therefore valid for acoustic waves that are long compared to the airfoil thickness but short compared to its chord. Furthermore, the acoustic compactness of the computational domain in the spanwise direction is exploited to simplify the calculation. A detailed discussion of approximations and limitations of this formulation is given in Wang & Moin (2000). In the frequency domain the acoustic pressure in the far field is approximately

$$\widehat{p}_a(\mathbf{x},\omega) \approx \frac{e^{i\left(k|\mathbf{x}|-\frac{\pi}{4}\right)}}{2^{\frac{5}{2}}\pi^{\frac{3}{2}}\,|\mathbf{x}|}\,(k\sin\phi)^{\frac{1}{2}}\sin\frac{\theta}{2}\;\widehat{S}(\omega),$$

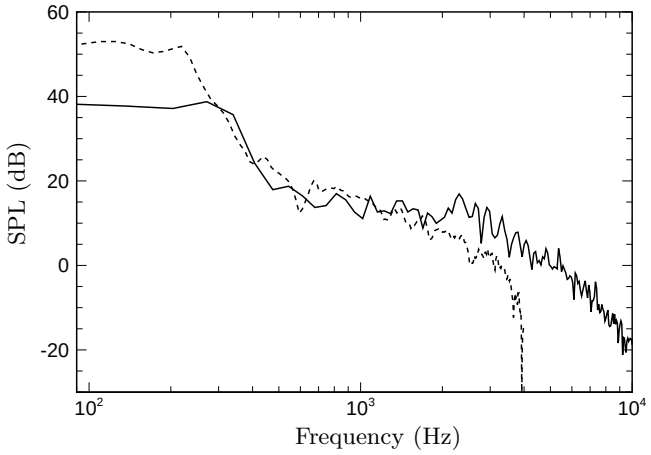


FIGURE 9. Comparison of computed and experimental sound pressure spectra: ——— , LES; - - - - , Experiment (Olson & Mueller 2004). The computational result is a spatial average of the acoustic spectra over an acoustic array plane centered at $x/h = 3$, $y/h = 21$. The experimental data are based on the cross-spectrum of two acoustic arrays positioned on opposite sides of the trailing edge.

where

$$S(t) = \int_V \frac{\rho_0}{r_0^{\frac{3}{2}}} \left\{ \left(u_\theta^2 - u_r^2\right) \sin\frac{\theta_0}{2} - 2u_r u_\theta \cos\frac{\theta_0}{2} \right\} d^3\mathbf{y}.$$

In the above equations $\mathbf{x} = (r, \theta, z)$ and $\mathbf{y} = (r_0, \theta_0, z_0)$ represent far-field and source-field positions, respectively. The velocity components $u_r$ and $u_\theta$ are defined in a cylindrical-polar coordinate system, where the $z$ coordinate coincides with the trailing edge and $\theta$ is measured counter-clockwise from the downstream direction. The caret denotes temporal Fourier transform, $\omega$ is the circular frequency, $k = \omega/c_0$ is the acoustic wavenumber, and $\sin\phi = r/|\mathbf{x}|$.

A comparison of the computed and experimental sound pressure spectra is shown in Fig. 9. The computed spectrum represents the spatial average over an acoustic array plane centered at $x/h = 3$, $y/h = 21$. The experimental spectrum is from Olson & Mueller (2004) and is based on the cross-spectrum of two acoustic arrays positioned on opposite sides of the trailing edge, sampled at 8 kHz with a 4 kHz filter. Our numerical prediction is in good agreement with the experimental data for approximately one decade of frequencies. The large discrepancy observed at low frequencies is caused by a number of factors. At frequencies below 300 Hz, the measurement plane is within one acoustic wavelength from the trailing edge, and the spacing between array micro-phones is also smaller than the wavelength. As a result, the measured spectrum may contain large near-field effects and noise from extraneous sources not included in the computation. More recent work of Shannon & Morris (personal communication) confirms that the low frequency portion of the experimental spectrum is dominated by noise from the collector. The numerical solution is likewise problematic in the low frequency range because the approximations about acoustic far-field and half-plane Green's function are formally invalid. Furthermore, in evaluating the noise radiated from the entire span of the airfoil, we have assumed that the aeroacoustic sources outside the computational

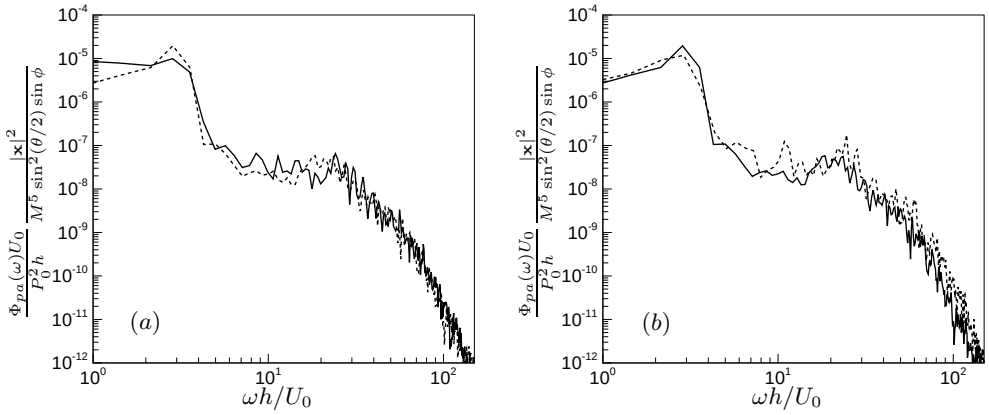


FIGURE 10. Dimensionless sound pressure spectra in the far field as a function of frequency illustrating the effects of (*a*) spanwise domain size (——— , $L_z = h$; - - - - , $L_z = h/2$) and (*b*) flow condition (——— , in open-jet facility; - - - - , in free stream). Dependence on observer location is absorbed into the spectra based on the far-field directivity of a half-plane.

domain in the spanwise direction are statistically independent, which is not true at low frequencies because of the small computational domain size.

Finally, the effects of the spanwise domain size and flow conditions on the predicted far-field noise are investigated. As shown in Fig. 10*a*, the far-field noise spectra computed using $L_z = h$ and $L_z = h/2$ indicate a relatively low sensitivity to the spanwise domain size. The small-domain result shows a stronger peak at the vortex shedding frequency, but the overall acoustic power remains approximately the same. Figure 10*b* compares the noise spectra computed with flow conditions in the Notre Dame open-jet facility and in a uniform free stream (Marsden *et al.* 2005). The variations are again small. These results provide justifications for the trailing-edge aeroacoustic optimization work of Marsden *et al.* (2005) which, because of the large computational expense, was performed in the smaller spanwise domain in a uniform free stream.

## 3. Concluding remarks

This report summarizes a computational study of the noise generated by the flow past an asymmetric trailing edge which is sufficiently blunt to cause vortex shedding. Large-eddy simulation is employed to compute the source field, and the acoustic far field is computed using Lighthill's theory. The flow and acoustic results are validated against the experimental measurements of Olson & Mueller (2004). Despite some remaining issues with velocity boundary conditions, LES predicts the correct overall features of the vortex-shedding trailing-edge flow. A direct comparison is made between the computed and measured sound pressure spectra, and good agreement is achieved in the intermediate frequency range of approximately one decade.

The experimental work is presently continuing at the University of Notre Dame, and refined acoustic data will be forthcoming. An exact match between the experimental and computational flow conditions remains a significant challenge due to experimental and numerical uncertainties. Validation of computational approaches and verification of simulation results require patience and thoroughness, and a close collaboration with experimentalists can greatly facilitate this process. From a computational perspective,

further improvement in accuracy is desired to extend the frequency range of validity of the predicted acoustic field. This requires more exact representations of acoustic source functions and the Green's function. A numerical evaluation of the acoustic Green's function will be pursued in the future, which will allow for a full account of the acoustic diffraction by the airfoil.

## Acknowledgments

This work was supported by the Office of Naval Research under grant Nos. N00014-01-1-0423 and N00014-04-1-0386. Computer time was provided by DoD's HPCMP through ASC/MSRC and by NAS at NASA Ames Research Center. We are grateful to Thomas Mueller, Scott Morris, Susan Olson and Daniel Shannon for providing the experimental data and related assistance, Gianluca Iaccarino for performing the RANS calculations, and William K. Blake for his active interest and helpful comments during the course of this work.

## REFERENCES

Blake, W. K. 1975 A Statistical Description of Pressure and Velocity Fields at the Trailing Edge of a Flat Strut. *DTNSRDC Report 4241*, David Taylor Naval Ship R & D Center, Bethesda, Maryland.

Ffowcs Williams, J. E. & Hall, L. H. 1970 Aerodynamic sound generation by turbulent flow in the vicinity of a scattering half plane. *J. Fluid Mech.* **40**, 657–670.

Howe, M. S. 1978 A review of the theory of trailing edge noise. *J. Sound Vib.* **61**, 437–465.

Lighthill, M. J. 1952 On sound generated aerodynamically; I. General theory. *Proc. Roy. Soc. London Ser. A* **211**, 564–587.

Lund, T. S., Wu, X. & Squires, K. 1998 Generation of turbulent inflow data for spatially-developing boundary layer simulations. *J. Comput. Phys.* **140**, 233–258.

Manoha, E., Troff, B. & Sagaut, P. 2000 Trailing edge noise prediction using large eddy simulation and acoustic analogy. *AIAA J.* **38**, 575–583.

Marsden, A. L., Wang, M., Dennis, J. E. & Moin P. 2005 Trailing-edge noise reduction using large-eddy simulation and derivative-free optimization. In preparation.

Moreau, S., Henner, M., Iaccarino, G., Wang, M. & Roger, M. 2003 Analysis of flow conditions in free-jet experiments for studying airfoil self-noise. *AIAA J.* **41**, 1895–1905.

Oberai, A. A., Roknaldin F. & Hughes T. J. R. 2002 Computation of trailing-edge noise due to turbulent flow over an airfoil. *AIAA J.* **40**, 2206–2216.

Olson, S. & Mueller T. J. 2004 An Experimental Study of Trailing Edge Noise. *Tech. Report UNDAS-IR-0105*, Dept. of Aerospace and Mechanical Engineering, Univ. of Notre Dame, Notre Dame, Indiana.

Wang, M. & Moin, P. 2000 Computation of trailing-edge flow and noise using large-eddy simulation. *AIAA J.* **38**, 2201–2209.

Wang, M., Moreau, S., Iaccarino, G. & Roger, M. 2004 LES prediction of pressure fluctuations on a low speed airfoil. *Annual Research Briefs 2004*, Center for Turbulence Research, NASA Ames/Stanford Univ., 183–193.